Chapter 15

Theory and Computer Simulation of Structure, Transport, and Flow of Fluid in Micropores

H. T. Davis, I. Bitsanis, T. K. Vanderlick, and M. V. Tirrell

Chemical Engineering and Materials Science Department, University of Minnesota, Minneapolis, MN 55455

An overview is given of recent progress made in our laboratory on this topic. The density profiles of fluid in micropores are found by solving numerically an approximate Yvon-Born-Green equation. A related local average density model (LADM) allows prediction of transport and flow in inhomogeneous fluids from density profiles. A rigorous extension of the Enskog theory of transport is also outlined. Simple results of this general approach for the tracer diffusion and Couette flow between planar micropore walls are presented. Equilibrium and flow (molecular dynamics) simulations are compared with the theoretical predictions. Simulated density profiles of the micropore fluid exhibit substantial fluid layering. The number and sharpness of fluid layers depend sensitively on the pore width. The solvation force and the pore average density and diffusivity are oscillating functions of the pore width. The theoretical predictions for these quantities agree qualitatively with the simulation results. The flow simulations indicate that the flow does not affect the fluid structure and diffusivity even at extremely high shear rates ($10^{10}s^{-1}$). The fluid structure induces large deviations of the shear stress and the effective viscosity from the bulk fluid values. The flow velocity profiles are correlated with the density profiles and differ from those of a bulk fluid. The LADM and extended Enskog theory predictions for the velocity profiles and the pore average diffusivity agree very well with each other and with the simulation results. The LADM predictions for the shear stress and the effective viscosity agrees fairly well with the simulation results.

Examples of fluids confined in pores and spaces of molecular or nanometer dimensions abound in technological and natural products and processes. These include wetting and lubrication, zeolite supported catalysis, silica gel based chromatrographic separations, drying of paper

0097-6156/87/0353-0257$07.25/0

products and clay dispersions, aggregation of colloids, permeation of Vicor and other sintered glasses, the formation of soap films, foams and emulsions, and water or oil rich zones in lyotropic liquid crystals and vesicular bilayer structures. In such confinement the fluids can be strongly inhomogeneous and so the usual theories of fluid structure and dynamics may not be applicable. Owing to the molecular dimensions involved, experimental characterization of fluid in micropores is also difficult. Thus, computer simulation on model systems becomes an important tool to test ideas and supplement experiments on real systems in trying to understand the behavior of fluids confined on the nanometer scale.

In this paper, we report recent progress made in our laboratory in using molecular theory and computer simulation to understand the structure, flow and transport of fluids confined by planar solid walls separated by a few molecular diameters.

Molecular Theory of Structure and Transport

Equilibrium Theory of Fluid Structure. In all the theoretical work reported herein, we assume that the particles interact with pair additive forces whose pair potentials can be approximated by

$$u(s) = u_R(s) + u_A(s) \tag{1}$$

where

$$u_R(x) = \infty, \quad s < \sigma$$
$$= 0, \quad s > \sigma \tag{2}$$

and $u_A(s)$ is the continuous, attractive part of the pair potential. The pore walls confining the fluid will be represented by the conservative potential $u^e(\mathbf{r})$. At equilibrium the density $n(\mathbf{r})$ of the fluid obeys the Yvon-Born-Green (YBG) equation

$$k_B T \nabla n + n \nabla u^e - n \int n(\mathbf{r}+\mathbf{s}) g(\mathbf{r}, \mathbf{r}+\mathbf{s}) \frac{\mathbf{s}}{s} u_A'(s) d^3 s$$

$$+ n k_B T \int n(\mathbf{r} + \sigma \mathbf{k}) g(\mathbf{r}, \mathbf{r} + \sigma \mathbf{k}) \sigma^2 \mathbf{k} d^2 k = 0 \tag{3}$$

where $g(\mathbf{r},\mathbf{r}')$ is the pair correlation function, k_B is Boltzmann's constant and T is the absolute temperature. $\mathbf{k}$ is a unit vector lying along the line of centers of a pair of molecules in contact. d^2k denotes an element of solid angle associated with $\mathbf{k}$.

Equation 3 is exact for fluids obeying Equations 1 and 2. However, in order to compute the density $n(\mathbf{r})$ from the YBG equation one must know the relationship between density distribution and the pair correlation function of inhomogeneous fluid. Such a relationship is not available in general. However, an approximation introduced by Fischer and Methfessel (1) has been shown to give fairly accurate predictions of the density

profiles in liquid-vapor and liquid-solid interfaces. It has also been shown that their approximation gives the exact density distribution for one-dimensional hard rods in an external potential u^e. The main assumption of Fischer and Methfessel is that the pair correlation function can be approximated as

$$g(\mathbf{r},\mathbf{r}+\mathbf{s}) = g^{\circ}(s;\bar{n}(\mathbf{r}+\frac{1}{2}\mathbf{s})) \tag{4}$$

where g° is the correlation function of homogeneous fluid and $\bar{n}$ is a local average density defined by

$$\bar{n}(\mathbf{r}) = \frac{1}{(\pi\sigma^3/6)} \int_{R<\sigma/2} n(\mathbf{r}+\mathbf{R})d^3R \tag{5}$$

Equation 4 renders the YBG equation solvable. However, as did Fischer and Methfessel we shall further simplify the theory by making the van der Waals' structureless fluid approximation ($g = 0$, $s < \sigma$, $g = 1$, $s > \sigma$) in the integral involving the long-ranged continuous force u_A'. The YBG equation thus becomes

$$\nabla[k_BT\ln n + u^e + \int n(\mathbf{r}+\mathbf{s})u_A(s)d^3s]$$

$$+ k_BT\int g^{\circ}(\sigma;\bar{n}(\mathbf{r}+\frac{\sigma}{2}\mathbf{k})\sigma^2\mathbf{k}d^2k = 0 \tag{6}$$

To finally complete the model a formula for the contact value of the pair correlation function g° must be given. We choose the Carnahan formula

$$g^{\circ}(\sigma;\bar{n}) = \frac{1-\frac{\pi}{12}\sigma^3\bar{n}}{(1-\frac{\pi}{6}\sigma^3\bar{n})^3} \tag{7}$$

shown by Carnahan and Starling (2) to be accurate in hard sphere fluids.

In the calculations to be reported in what follows we shall consider planar systems, i.e., flat pore walls so that $u^e = u^e(x)$ and $n = n(x)$, where x is the distance from a pore wall. In this case Equation 6 can be integrated to give

$$\mu^* = \ln n(x) + \frac{1}{k_BT}\int_{-\infty}^{+\infty} n(x')\bar{u}_A(x-x')dx'$$

$$+ 2\pi\sigma^2\int_0^x dx'\int_{-1}^{1} d\varsigma\varsigma n(x'+\sigma\varsigma)g(\bar{n}(x'+\frac{1}{2}\sigma\varsigma)) - \frac{u^e(x)}{k_BT} \tag{8}$$

where

$$\bar{n}(x) = (6/\sigma^3) \int_{-\sigma/2}^{+\sigma/2} (.25\sigma^2 - (x - x')^2) n(x') dx' \qquad (9)$$

The constant of integration μ^* is a field variable similar to the chemical potential ($\mu^* = -3.6227$ in our calculations).

The external potential, $u^e(x)$, arises from the solid walls at $x = 0$ and $x = h$.

$$u^e(x) = \phi_w(x) + \phi_w(h - x) \qquad (10)$$

where each wall exerts a 10-4-3 potential (3):

$$\phi_w = \epsilon_w \left[\left(\frac{2}{5}\right)\left(\frac{\sigma_w}{x}\right)^{10} - \left(\frac{\sigma_w}{x}\right)^4 - \frac{\sqrt{2}\sigma_w^3}{3(x + \frac{0.61\sigma_w}{\sqrt{2}})^3} \right], \quad x > 0 \qquad (11)$$

ϵ_w and σ_w are characteristic wall-fluid particle energy and separation distance parameters.

The fluid-fluid intermolecular potential,

$$\bar{u}_A(x) = \int_{-\infty}^{+\infty} \int u^A(s) dydz \qquad (12)$$

is taken to be

$$\begin{aligned} \bar{u}_A(x) &= -2\pi\epsilon\sigma^2, \quad |x| < \sigma \\ &= -\frac{2\pi\epsilon\sigma^6}{x^4}, \quad |x| > \sigma \end{aligned} \qquad (13)$$

This corresponds to the attractive part of a "6 - ∞" Lennard-Jones potential; namely,

$$\begin{aligned} u^A(s) &= -4\epsilon\left(\frac{\sigma}{s}\right)^6, \quad s > \sigma \\ &= 0, \quad s < \sigma \end{aligned} \qquad (14)$$

The normal pressure P_N in the fluid confined between the walls varies with wall separation and is not, in general, equal to the bulk pressure P_B of fluid at the same chemical potential. The difference $P_N - P_B$ is the solvation force per unit area, (4) f_s, and can be calculated from the equilibrium density profiles by

$$f_s = -\int_0^h n(x)\frac{d\phi_w(x)}{dx}dx + \int_0^\infty n(x)\frac{d\phi_w(x)}{dx}dx \qquad (15)$$

The equilibrium density profiles are obtained by solving Equations 8 and 9 for a modified density $n^*(x)$, where

$$n^*(x) = n(x)e^{u^e(x)/kT} \qquad (16)$$

This modified density is a more slowly varying function of x than the density. The domain of interest, $0 < x < h$, is discretized uniformly and the trapezoidal rule is used to evaluate the integrals in Equations 8 and 9. This results in a system of nonlinear, coupled, algebraic equations for the nodal values of n^* and $\bar{n}$. Newton's method is used to solve for n^* and $\bar{n}$ simultaneously. The domain is discretized finely enough so that the solution changes negligibly with further refinement. A mesh size of 0.05σ was adopted in our calculations.

Solutions were obtained initially for a wall separation $h = 40\sigma$, where at the midpoint the density is equal to the bulk fluid density, n_b. Then, solutions for decreasing pore width were found using the previous solution at larger h as a first guess for the next width. Pore width was gradually decreased to $h = 2.25\sigma$ using small enough steps to ensure that quadratic convergence was observed at each new pore width. Step sizes ranged from a few σ 's to 0.05σ.

Local Average Density Model (LADM) of Transport. In the spirit of the Fischer-Methfessel local average density model, Equation 4, for the pair correlation function of inhomogeneous fluid, a local average density model (LADM) of transport coefficients has been proposed (5) whereby the local value of the transport coefficient, $\lambda(\mathbf{r})$, is approximated by

$$\lambda(\mathbf{r}) = \lambda^\circ(\bar{n}(\mathbf{r})) \qquad (17)$$

$\lambda^\circ(\bar{n}(\mathbf{r}))$ is the transport coefficient of homogeneous fluid at the local average density $\bar{n}(\mathbf{r})$.

According to this model the diffusivity of a molecule at position x in the planar pore system of interest in this paper is $D^\circ(\bar{n}(x))$ and so the pore diffusivity is

$$D_{pore} = \int_0^h n(x)D^\circ(\bar{n}(x))dx \Big/ \int_0^h n(x)dx \qquad (18)$$

since $D^\circ(\bar{n}(x))n(x)Adx/N$ is the probable diffusivity of a particle lying between x and $x + dx$ in the pore.

The stress tensor $\boldsymbol{\tau}$ according to LADM is

$$\tau(\mathbf{r}) = \frac{\eta^{\circ}(\bar{n}(\mathbf{r}))}{2}\left[\nabla\bar{\mathbf{v}} + \nabla\bar{\mathbf{v}}^{T}\right] + \left[\eta_b^{\circ}(\bar{n}(\mathbf{r})) - \frac{2}{3}\eta^{\circ}(\bar{n}(\mathbf{r}))\right]\nabla\cdot\mathbf{v}\mathbf{I} \quad (19)$$

where $\bar{\mathbf{v}}$ is the mean flow velocity, $\nabla\bar{\mathbf{v}}^{T}$ is the transpose of $\nabla\bar{\mathbf{v}}$, $\eta^{\circ}(\bar{n})$ and $\eta_b^{\circ}(\bar{n})$ the shear and bulk viscosity coefficients of homogeneous fluid at density $\bar{n}$.

The attractive feature of LADM is that once the fluid structure is known (e.g., by solution of the YBG equations given in the previous section or by a computer simulation) then theoretical or empirical formulas for the transport coefficients of homogeneous fluids can be used to predict flow and transport in inhomogeneous fluid. For diffusion and Couette flow in planar pores LADM turns out to be a surprisingly good approximation, as will be shown in a later section.

Enskog Theory of Transport. Enskog's theory of hard spheres, with introduction of a temperature dependent hard sphere diameter, gives surprisingly accurate estimates of the diffusivity and viscosity of real fluids (6). This is because in simple fluids the short-ranged repulsive forces between molecules dominate in the collisional dissipation leading to transport phenomena. The long-ranged attractive interactions contribute importantly to the energy of the fluid, and thus to phase transitions and interfacial structure, but apparently are less effective in collisional dissipation. With this view of fluid behavior Enskog's theory of transport in bulk fluid has been generalized to strongly inhomogeneous fluids.

Consider a fluid of molecules interacting with pair additive, centrally symmetric forces in the presence of an external field and assume that the collisional contribution to the equation of motion for the singlet distribution function is given by Enskog's theory. In a multicomponent fluid, the distribution function $f_i(\mathbf{r},\mathbf{v}_i,t)$ of a particle of type i at position $\mathbf{r}$, with velocity $\mathbf{v}_i$ at time t obeys the equation of change (7)

$$\frac{\partial f_i}{\partial t} + \mathbf{v}_i\cdot\nabla f_i - \frac{1}{m_i}\nabla u_i^{e}\cdot\nabla_{\mathbf{v}_i} f_i$$

$$- \sum_j \frac{1}{m_i}\int \nabla u_{ij}^{A}(\mathbf{r}-\mathbf{r}')\cdot\nabla_{\mathbf{v}_i} f_i f_j g_i(\mathbf{r},\mathbf{r}',t)\,d^3r'd^3v_j$$

$$= \sum_j \int_{\mathbf{v}_{ji}\cdot\mathbf{k}>0} \left[g_{ij}(\mathbf{r},\mathbf{r}+\sigma_{ij}\mathbf{k}) f_i(\mathbf{r},\mathbf{v}_i',t) f_j(\mathbf{r}+\sigma_{ij}\mathbf{k},\mathbf{v}_j',t)\right.$$

$$\left. - g_{ij}(\mathbf{r},\mathbf{r}-\sigma_{ij}\mathbf{k}) f_i(\mathbf{r},\mathbf{v}_i,t) f_j(\mathbf{r}-\sigma_{ij}\mathbf{k},\mathbf{v}_j,t)\right]\sigma_{ij}^2\mathbf{v}_{ji}\cdot\mathbf{k}\,d^2k\,d^3v_j \quad (20)$$

where ∇ and $\nabla_{\mathbf{v}_i}$ are gradient operators with respect to $\mathbf{r}$ and $\mathbf{v}_i$, m_i molecular mass, u_i^{e} the potential of the external force, u_{ij}^{A} the pair potential of attractive forces between particles of types i and j, g_{ij} the pair correlation function between i and j, $\sigma_{ij} \equiv (\sigma_{ii} + \sigma_{jj})/2$, σ_{ii} the hard sphere diameter of i, $\mathbf{k}$ a unit vector directed from the center of i to that of j, and $\mathbf{v}_i'$ the velocity of i after a hard-sphere collision with j. We recall that

$\mathbf{v}_i' = \mathbf{v}_i - \mathbf{v}_{ij}\cdot\mathbf{kk}$, where $\mathbf{v}_{ij} \equiv \mathbf{v}_i - \mathbf{v}_j(\underline{7})$. The attractive interaction u_{ij}^A is assumed to be sufficiently slowly varying that it does not contribute to collisional dissipation.

The local density n_i of species i is related to the velocity distribution function by

$$n_i(\mathbf{r},t) = \int f_i(\mathbf{r},\mathbf{v}_i,t)d^3v_i \tag{21}$$

At equilibrium the distribution function is of the form

$$f_i = n_i(\mathbf{r})\phi_i(\mathbf{v}_i) \tag{22}$$

where ϕ_i is the Maxwell velocity distribution function,

$$\phi_i(\mathbf{v}_i) = \left(\frac{m_i}{2\pi k_B T}\right)^{3/2} \exp(-\, m_i v_i^2/2k_B T) \tag{23}$$

With this distribution function, velocity factors out of Equation 20 yielding the exact YBG equation, Equation 3, for equilibrium fluids whose interaction potential is given by Equation 1.

The Chapman-Enskog method has been used to solve for steady state tracer diffusion (8). According to the method the singlet distribution function for the diffusing species 1, present in a trace amount ($n_1 << n_i$, $i \neq 1$) in an otherwise equilibrium fluid, is approximated by

$$f_1 = n_i(\mathbf{r})\phi_1(\mathbf{v}_1)\,[\,1 + \mathbf{a}_1(\mathbf{r})\cdot\mathbf{v}_1\,] \tag{24}$$

and $\mathbf{a}_1(\mathbf{r})$ is obtained from the Enskog equation. The result for the linearized diffusion flux $\mathbf{J}_1$ of species 1:

$$\mathbf{J}_1 = \int f_1\mathbf{v}_1 d^3v_1 = -\, n_1^\circ k_B T \boldsymbol{\zeta}_1^{-1}\cdot\nabla \ln(n_1/n_1^\circ) \tag{25}$$

where $\boldsymbol{\zeta}_1$ is the friction tensor,

$$\boldsymbol{\zeta}_1(\mathbf{r}) = \sum_{j\neq 1}\frac{m_1}{\pi}\left(\frac{2\pi k_B T}{m_{1j}}\right)^{1/2}\int g_{1j}(\mathbf{r},\mathbf{r}+\sigma_{1j}\mathbf{k})n_j^\circ(\mathbf{r}+\sigma_{1j}\mathbf{k})\sigma_{1j}^2\mathbf{kk}d^2k \tag{26}$$

$m_{1j} \equiv m_1 m_j/(m_1+m_j)$, $g_{1j}(\mathbf{r},\mathbf{r}+\sigma_{1j}\mathbf{k})$ the equilibrium pair correlation function, $n_1^\circ(\mathbf{r})$ the equilibrium density distribution of species 1, and $n_1(\mathbf{r})$ the diffusive density distribution.

As expected from continuum theory, the friction and diffusion coefficients are replaced in inhomogeneous fluid by tensors whose symmetry reflects that of the inhomogeneous media.

For the special case of self-diffusion (tracer molecules dynamically

identical to solvent molecules) in the y-direction in a planar pore, it follows from Equation 25 that the pore average flux obeys (9)

$$J_{pore} = \frac{1}{h}\int_0^h J_{1y}dx = - D_{pore}\frac{dn_{pore}}{dx} \tag{27}$$

where $n_{pore} = h^{-1}\int_0^h n_1 dx$ and

$$D_{pore} = \int_0^h D_T(x)n^\circ(x)dx / \int_0^h n^\circ(x)dx \tag{28}$$

$D_T(x)$, the local diffusivity parallel to the pore walls, is given by

$$D_T(x) = \frac{(k_B T/\pi m)^{1/2}}{4\sigma^2\int_{-1}^{1} g^\circ(\sigma, \bar{n}^\circ(x + \frac{\sigma}{2}\xi))n^\circ(x + \sigma\xi)(1 - \xi^2)d\xi} \tag{29}$$

a result enabling one to calculate the pore diffusivity from the equilibrium density distribution function.

Equation 28 is similar to the LADM formula for pore diffusivity, except that in LADM $D_T(x)$ is replaced by

$$D^\circ(\bar{n}(x)) = \frac{(k_B T/\pi m)^{1/2}}{(8\sigma^2/3)g^\circ(\sigma, \bar{n}(x))\bar{n}(x)} \tag{30}$$

The Chapman-Enskog theory of flow in a one-component fluid yields the following approximation to the momentum balance equation (10).

$$n\partial_t \bar{\mathbf{v}} + n\bar{\mathbf{v}}\cdot\nabla\bar{\mathbf{v}} + \frac{n}{m}\nabla u^e - \nabla\cdot\mathbf{P} = - \mathbf{M}_1 : \nabla\bar{\mathbf{v}} + \mathbf{M}_2 \vdots \nabla\nabla\bar{\mathbf{v}} \tag{31}$$

where $\mathbf{P}$ is the local pressure tensor and $\mathbf{M}_1$ and $\mathbf{M}_2$ are third and fourth rank tensors accounting for viscous dissipation. In isotropic fluid $\mathbf{P} = P\mathbf{I}$, $\mathbf{I}$ the unit tensor, $\mathbf{M}_1 = 0$ and $\mathbf{M}_2$ is a fourth rank isotropic tensor. The symmetries of $\mathbf{P}$, $\mathbf{M}_1$ and $\mathbf{M}_2$ depend on the symmetry of the inhomogeneous fluid. The general Chapman-Enskog formulas for $\mathbf{M}_1$ and $\mathbf{M}_2$ are very complicated and will not be recorded here. However, if the deviation of the velocity distribution function from its local Maxwellian form ($\phi = (m/2\pi k_B T)^{3/2} \exp[- m(\mathbf{v} - \bar{\mathbf{v}}(r))^2/k_B T]$) is neglected, the following relatively simple formulas are obtained (10)

$$\mathbf{M}_1(\mathbf{r}) = \left(\frac{mk_BT}{\pi}\right)^{1/2} \sigma^3 n(\mathbf{r}) \int n(\mathbf{r}+\sigma\mathbf{k}) g(\mathbf{r},\mathbf{r}+\sigma\mathbf{k}) \mathbf{kkk} d^2k \quad (32)$$

$$\mathbf{M}_2 = \left(\frac{mk_BT}{\pi}\right)^{1/2} \sigma^4 n(\mathbf{r}) \int n(\mathbf{r}+\sigma\mathbf{k}) g(\mathbf{r},\mathbf{r}+\sigma\mathbf{k}) \mathbf{kkkk} d^2k \quad (33)$$

These formulas become increasingly better approximations as the density increases (11).

For the steady, planar Couette flow to be examined in a later section, the momentum balance equation yields

$$n\frac{du^e}{dx} + \frac{dP_N}{dx} = 0 \quad (34)$$

and

$$0 = M_1(x)\frac{\partial \bar{v}_y}{\partial x} + M_2(x)\frac{\partial^2 \bar{v}_y}{\partial x^2} \quad (35)$$

where

$$M_1(x) = 2(\pi m k_B T)^{1/2} \sigma^3 n(x) \int_{-1}^{1} n(x+\sigma\xi) g(\sigma; x, x+\sigma\xi)(1-\xi^2)\xi d\xi \quad (36)$$

$$M_2(x) = (\pi m k_B T)^{1/2} \sigma^4 n(x) \int_{-1}^{1} n(x+\sigma\xi) g(\sigma; x, x+\sigma\xi)(1-\xi^2)\xi^2 d\xi \quad (37)$$

It can be shown that Equation 34 is the YBG equation determining the density distribution n(x) of the fluid. With the Fischer-Methfessel closure, the density distribution is all that is needed to calculate the coefficients $M_1(x)$ and $M_2(x)$. Integrating Equation 35, we find

$$\bar{v}_y(x) = \bar{v}_y(o) + [\bar{v}_y(h) - \bar{v}_y(o)] \frac{\int_o^x dx'' Q(x'')}{\int_o^h dx'' Q(x'')} \quad (38)$$

where

$$Q(x'') = \exp\left[-\int_o^{x''} dx' M_1(x')/M_2(x')\right] \quad (39)$$

LADM also leads to Equation 35, but with $M_1 = d\eta^\circ(\bar{n}(x))/dx$ and $M_2 = \eta^\circ(\bar{n}(x))$, which yields

$$\bar{v}_y(x) = \bar{v}_y(o) + [\bar{v}(h) - \bar{v}_y(o)] \frac{\int_o^x dx''[\eta^\circ(\bar{n}(x''))]^{-1}}{\int_o^h dx''[\eta^\circ(\bar{n}(x''))]^{-1}} \tag{40}$$

The theories of structure and transport outlined above will be compared with molecular dynamics in what follows.

Molecular Dynamics

Equilibrium Simulation. The equilibrium simulations described here were carried out by Magda *et al.* (12). The pore walls modelled are two flat, semi-infinite solids separated by a distance h in the x-direction. The wall-fluid potential is the 10-4 or 10-4-3 potential, i.e.,

$$\phi_w(x) = \epsilon_w \left\{ 0.4(\sigma_w/x)^{10} - (\sigma_w/x)^4 + \frac{\sqrt{2}\delta}{3(x/\sigma_w + 0.61/\sqrt{2})^3} \right\} \tag{41}$$

where $\delta = 1$ in some simulations and $\delta = 0$ in others. The particle-particle potential energy is chosen to be the truncated 6-12 Lennard-Jones potential

$$\begin{aligned} u(r) &= \phi_{LJ}(r) - \phi_{LJ}(r_e), \quad r < r_e \\ &= 0, \quad r > r_e \end{aligned} \tag{42}$$

where

$$\phi_{LJ}(r) = 4\epsilon \left[\left(\frac{\sigma}{r} \right)^{12} - \left(\frac{\sigma}{r} \right)^6 \right] \tag{43}$$

ϵ and σ are energy and particle size parameters and r_e is the truncation distance (typically taken to be 2.5 to 3.5σ in computer simulations).

The temperature, pore width and average pore densities were the same as those used by Snook and van Megen in their Monte Carlo simulations, which were performed for a constant chemical potential (13). Periodic boundary conditions were used in the y and z directions. The periodic length was chosen to be twice r_e. Newton's equations of motion were solved using the predictor-corrector method developed by Beeman (14). The local fluid density was computed form

$$n(x) = \frac{1}{A}\frac{dN}{dx}(0 \rightarrow x) \tag{44}$$

where A is the area of a pore wall and $N(0 \rightarrow x)$ is the long time average of the number of molecules found between 0 and x. The normal pressure exerted by the fluid on the pore wall was computed from

$$P_N = \frac{1}{2A} < - \sum_{i=1}^{N} \frac{du^e(x_i)}{dx} >$$

$$= - \frac{1}{2}\int_0^h n(x)\frac{du^e(x)}{dx}dx \tag{45}$$

or the Irving-Kirkwood pressure tensor mentioned below (15). <---> denotes an ensemble average or a long-time average (used in molecular dynamics).

The self-diffusion coefficient parallel to the pore walls was computed form the mean square particle displacement,

$$D_{pore} = \lim_{t \rightarrow \infty} \frac{1}{N}\sum_{i=1}^{N}\frac{1}{4t} < [y_i(t) - y_i(0)]^2 + [z_i(t) - z_i(0)]^2 > \tag{46}$$

and the Green-Kubo formula

$$D_{pore} = \frac{1}{2}\int_0^\infty [\psi_y(t) + \psi_z(t)]\,dt \tag{47}$$

where the velocity autocorrelation function $\psi_\nu(t)$ is defined by

$$\psi_\nu(t) \equiv \frac{1}{N}\sum_{i=1}^{N} < v_{i\nu}(t)v_{i\nu}(0) > \ , \ \nu = x, y, \text{ or } z \tag{48}$$

Couette Flow Simulation. MD typically simulate systems at thermodynamic equilibrium. For the simulation of systems undergoing flow various methods of nonequilibrium MD have been developed (16, 17). In all of these methods the viscosity is calculated directly from the constitutive equation.

The nonequilibrium MD method we employed (5) is the reservoir method (16) which simulates plane Couette flow. The effective viscosity is calculated from the constitutive relation

$$\tau_{xy} = \eta_{eff}\dot{\gamma}_{imp} \tag{49}$$

where τ_{xy} is the xy component of the stress tensor, η_{eff} an effective coefficient of shear viscosity, $\dot{\gamma}_{imp}$ is the imposed shear rate.

In this method the liquid of interest is sheared between two semi-infinite reservoirs. The reservoirs contain particles identical with the ones in the main liquid slab and at the same density. The reservoir particles and the particles of the main liquid slab interact by exerting forces on each other but they do not mix because they are separated by impenetrable hard walls extending on the yz plane. Therefore, the reservoirs are fluid-like and confine the main liquid slab in the x direction. Despite appearances, the main liquid slab behaves like a bulk fluid because the reservoirs induce no significant structure in the confined liquid. Furthermore, the hard impenetrable reservoir walls are not to be confused with the flat 10-4 LJ pore walls mentioned in the previous subsection.

The flow is induced in the following way. External forces are applied on the particles of each reservoir in order to keep the average y velocities of the reservoirs constant. The imposed motion of the reservoirs shears the liquid slab. The work supplied in order to keep the reservoirs moving eventually is dissipated and heats up the liquid. In order to remove this extra heat from the system the velocities of the reservoir molecules are scaled at each time step so as to keep the average reservoir temperatures constant. The imposed shear rate is obviously

$$\dot{\gamma}_{imp} = (\bar{v}_{y,u} - \bar{v}_{y,l})/s \qquad (50)$$

where, $\bar{v}_{y,u}$ is the average velocity of the upper reservoir particles, $\bar{v}_{y,l}$ the average velocity of the lower reservoir particles, and s the width of the main liquid slab.

Depending on the density in the vicinity of the reservoir walls some slip might be observed. Therefore, the actual shear rate that the liquid slab experiences might be lower than the imposed one. This actual shear rate $\dot{\gamma}$ is determined empirically from the simulation by calculating the average velocity of the liquid slab particles which are located next to the reservoir walls. The actual shear rate $\dot{\gamma}$ rather than the imposed shear rate $\dot{\gamma}_{imp}$ is to be used in Equation 49 for the calculation of the effective viscosity η_{eff}.

The structure is induced by a pore wall potential, which has the form of the potential used in the equilibrium simulations (Equation 41) with $\delta = 0$, $\epsilon_w = 4\epsilon$ and $\sigma_w = \sigma$, (ϵ, σ are the parameters of the truncated 12-6 LJ potential of the pair interactions of particles in the main liquid slab and the reservoirs.)

The arrangement described above allows one to turn off the flow and/or the wall potential at will and, therefore, to simulate bulk fluid and fluid confined between planar micropore walls both at equilibrium and under flow.

We simulated two systems: (1) bulk fluid (no wall potential) at equilibrium and undergoing Couette flow, and (2) fluid confined between planar micropore walls at equilibrium and undergoing Couette flow.

The location of the pore walls does not coincide with the location of the reservoir walls that confine the particles of the main liquid slab. This was done in order to minimize the slip at the reservoir walls as explained in detail in Reference (5).

In the flow simulations we address the following issues:

- the effect of density structure on the flow properties, such as the flow velocity profile, the shear stress and the viscosity, by comparing the bulk and the structured systems under flow.
- the effect of flow on the density structure and the diffusivity by comparing the density profiles and the diffusivities of both systems at equilibrium and under flow. Furthermore, we compare the two diffusivities on the plane parallel to the reservoir walls, i.e., the diffusivity in the direction of flow and the one normal to the flow, for both systems undergoing flow.
- the effect of structure on the diffusivity by comparing the diffusivities of the structured and the bulk system at equilibrium.

The density profile for the micropore fluid was determined as in the equilibrium simulations. In a similar way the flow velocity profile for both systems was determined by dividing the liquid slab into ten slices and calculating the average velocity of the particles in each slice. The velocity profile for the bulk system must be linear as macroscopic fluid mechanics predict.

The diffusivities parallel to the pore walls at equilibrium were determined form the mean square particle displacements and the Green-Kubo formula as described in the previous subsection. The Green-Kubo Formula cannot be applied, at least in principle, for the calculation of the diffusivity under flow. The diffusivity can be still calculated from the mean square particle displacements provided that the part of the displacement that is due to the macroscopic flow is excluded. The presence of flow in the y direction destroys the symmetry on the yz plane. Hence the diffusivities in the y direction (parallel to the flow) and the z direction (normal to the flow) can in principle be different. In order to calculate the diffusivities the part of the displacement that is due to the flow must of course be excluded. Therefore,

$$D_{y,pore} = \lim_{t \to \infty} \frac{1}{N} \sum_{i=1}^{N} \frac{1}{2t} < [y_i(t) - \bar{v}t - y_i(0)]^2 > \qquad (51)$$

where $\bar{v}$ is the flow velocity at the location of particle i and

$$D_{z,pore} = \lim_{t \to \infty} \frac{1}{N} \sum_{i=1}^{N} \frac{1}{2t} < [z_i(t) - z_i(0)]^2 > \qquad (52)$$

since there is no flow in the z direction.

The shear stress is uniform throughout the main liquid slab for Couette flow (5). Therefore, two independent methods for the calculation of the shear stress are available; it can be calculated either from the y component of the force exerted by the particles of the liquid slab upon each reservoir or from the volume average of the shear stress developed inside the liquid slab from the Irving-Kirkwood formula (15). For reasons explained in Reference (5) the simpler version of this formula can be used in both our systems although this version does not apply in general to structured systems. The Irving-Kirkwood expression for the xy component of the stress tensor used in our simulation is

$$\bar{\tau}_{xy} V_{pore} = < \sum_{i=1}^{N_l} m v_{x,i} (v_{y,i} - \bar{v}_y(y_i)) + \frac{1}{2} \sum_{j,k=1}^{N} (x_j - x_k) F_{kj}^{(y)} + \sum_{j=1}^{N_r} \sum_{k=1}^{N_l} (x_k - x_{GDS}) F_{kj}^{(y)} \quad (83)$$

where, $\bar{\tau}_{xy}$ is the average shear stress over the main liquid slab
V_{pore} is the volume of the main liquid slab.
N_l is the number of particles in the main liquid slab
N_r is the number of particles in both reservoirs.
$v_{x,i}, v_{y,i}$ are the x and y components of the velocity of particle i
$\bar{v}_y(y_i)$ is the y component of the flow velocity at the current position of particle i
x_i, y_i are the x and y coordinates of particle i
x_{GDS} is the location of the Gibbs dividing surface between the main liquid slab and the reservoirs.

Discussion of Results

Equilibrium Systems. Magda *et al.* (12) have carried out an equilibrium molecular dynamics (MD) simulation on a 6-12 Lennard-Jones fluid in a slit pore described by Equation 41 with $\delta = 1$ with fluid particle interactions given by Equation 42. They used the Monte Carlo results of Snook and van Megen to set the mean pore density so that the chemical potential was the same in all the simulations. The parameters and conditions set in this work were $\epsilon_w = 2\pi\epsilon$, $\sigma_w = \sigma$, $r_e = 3.5\sigma$, $kT/\epsilon = 1.2$, and $n_b\sigma^3 = 0.5925$. ϵ and σ are the Lennard-Jones parameters of the fluid and n_b is the density of a bulk phase in equilibrium with the pore fluid.

To compare molecular theoretical and molecular dynamics results, we have chosen the same wall-particle potential but have used the 6 - ∞ fluid particle potential, Equation 14, instead of the truncated 6-12 LJ potential. This is done because the molecular theory is developed in terms of attractive particles with hard sphere cores. The parameter μ^* in Equation 8 is chosen so that the density of the bulk fluid in equilibrium with the pore fluid is the same , $n_b\sigma^3 = 0.5925$, as that in the MD simulations.

Figure 1 typifies the agreement found between the fluid density profiles predicted by Equation 8 and that obtained in the MD simulations. For this example the porewidth equals 4σ. The fluid density distribution has three large peaks (the maximum bulk density possible for a Carnahan-Starling fluid is $n_b\sigma^3 = 6/\pi \approx 1.9$) indicating a strong layering effect of the pore walls on the confined fluid.

The number and sharpness of fluid layers depend sensitively on the porewidth as is illustrated by the theoretical results (which agree qualitatively with simulations) plotted in Figure 2. As porewidth is increased from say $h = \sigma$, there appear one, two, three, etc. density peaks. A transition from N to N + 1 peaks occurs as the porewidth varies from a value at which N layers are favored to a value at which N + 1 are favored. A

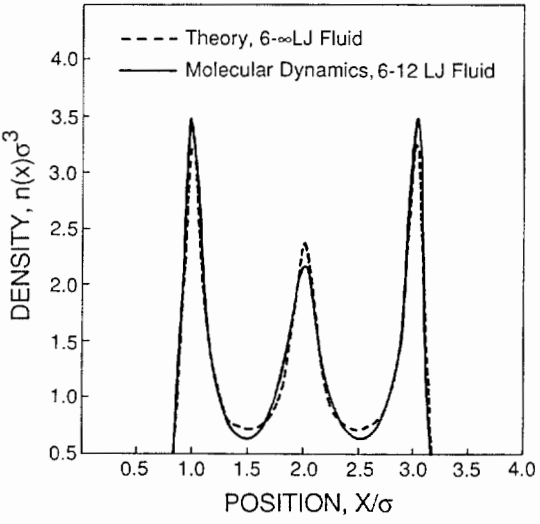

Figure 1. Fluid density versus distance from pore wall.

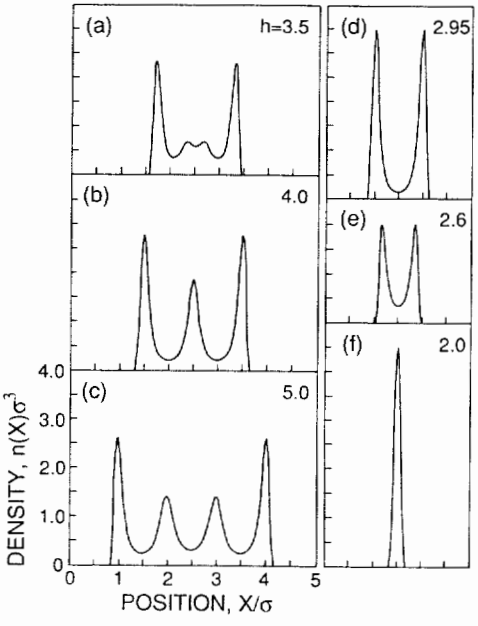

Figure 2. Density profiles illustrating effect of pore width on layering structure. Theory with 6 - ∞ LJ fluid.

quantity which measures this tendency is the so-called restricted pore average density.

$$n_{ave} = \frac{1}{h - 2\Delta} \int_0^h n(x)dx \tag{54}$$

where Δ is the thickness of the region near the pore wall which is empty of particles ($\Delta = 0.8\sigma$ for the wall potential used here). Predicted and simulated values of n_{ave} are plotted in Figure 3. n_{ave} has local maxima where a given number N of layers is favored and local minima where this number is not favored. For example, one layer is favored at $h = 1.95\sigma$ and two layers are favored at $h = 2.95\sigma$, as witnessed by local maxima in n_{ave}, whereas the local minimum between 1.95 and 2.95σ indicates a defective layering 1.95 and 2.95σ state in which neither one nor two layers are optimal. This behavior can be seen in Figure 2 in which the two density peaks decrease dramatically as the pore width is decreased from $h = 2.95\sigma$ to 2.60σ.

In the simulations the maxima and minima of n_{ave} are shifted to slightly smaller porewidths compared to predictions of the theory. This trend is consistent with the fact that the 6-12 Lennard-Jones potential is not infinitely repulsive at an interparticle separation of σ, whereas the 6-∞ potential is infinitely repulsive at σ.

It is now well established experimentally that the solvation force, f_s, of confined fluid is an oscillating function of pore wall separation. In Figure 4 we compare the theoretical and MD results for f_s as a function of h. Given that pressure predictions are very demanding of a molecular theory, the observed agreement between our simple theory and the MD simulations must be viewed as quite good. The local maxima and minima in f_s coincide with those in n_{ave} and therefore also reflect porewidths favorable and unfavorable to an integral number of fluid layers.

Similarly, the pore diffusivity D_{pore} (Figure 5) has local maxima and minima resulting from the layering structure of the confined fluid. As one might expect the local maxima and minima in D_{pore} coincide with the minima and maxima in n_{ave}.

In Figure 5, the MD results are compared with predictions of the Vanderlick-Davis extension of Enskog's theory and with LADM predictions using for D° the Enskog formula, Equation 30, and the theoretical density profile. The extended Enskog theory and LADM agree quite well with one another and are in qualitative agreement with the MD results. The maxima and minima of the MD results are shifted to smaller porewidths because of the softer core of the 6-12 LJ potential as compared to the 6-∞ potential. For the same reason, the bulk diffusivities of the theories are lower than that of the simulation. If, as is done in applying the Enskog theory of bulk phase transport coefficients to real fluids, we choose for the 6-∞ model an effective diameter σ_{eff} the agreement between theory and simulation can be improved. For example, with $\sigma_{eff} = 0.972\sigma$ Enskog's diffusivity of bulk fluid agrees with the simulation and improved agreement pore diffusivities result (Figure 6).

Beyond a porewidth of about 12σ, the theory and the MD results

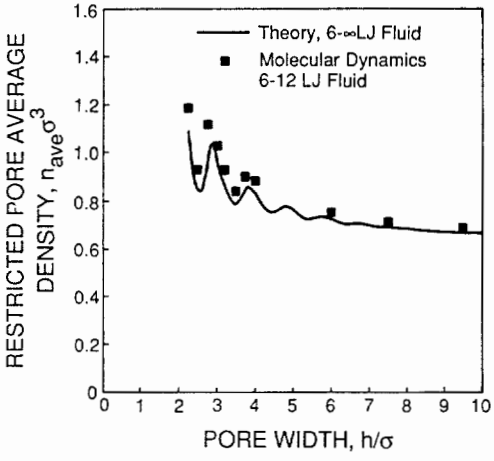

Figure 3. Molecular dynamics results for restricted pore average density versus pore width.

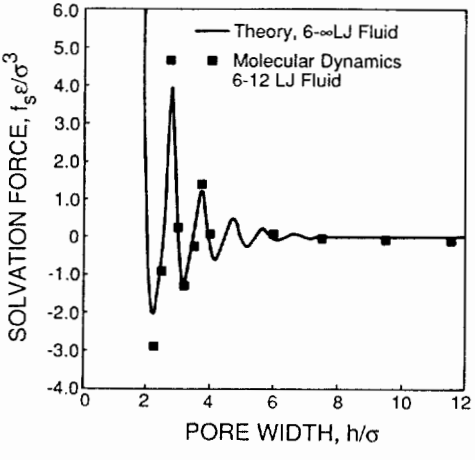

Figure 4. Molecular dynamics results for solvation force versus pore width.

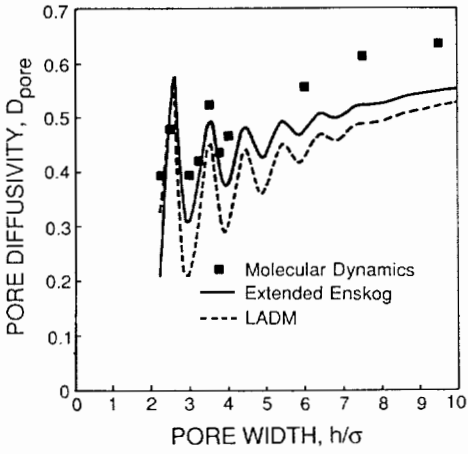

Figure 5. Pore diffusivity versus pore width. Theory is for 6-∞ LJ fluid. Units of diffusivity are $(3\sigma/8)(k_BT/\pi m)^{1/2}$.

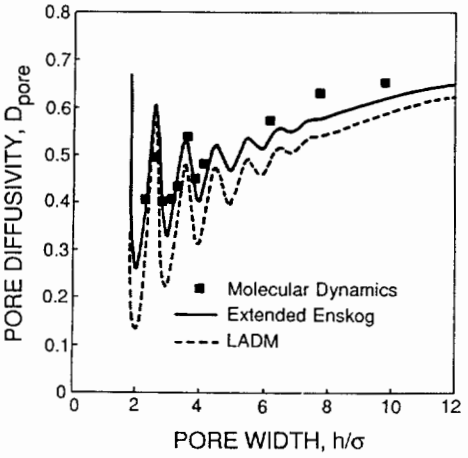

Figure 6. Pore diffusivity versus pore width. Theory is for 6-∞ LJ fluid with an effective hard sphere diameter $\sigma_{eff} = 0.972$. Units of diffusivity are $(3\sigma/8)(k_BT/\pi m)^{1/2}$.

agree that the fluid profile is fully developed at each pore wall and further wall separation simply recruits more almost bulk fluid the middle region of pore with very little change in the density profile of the four or five layers near the pore wall.

Flow systems. In this subsection we present the results of our Couette flow simulations. Most of these results were first presented in Reference (5).

i) *Density profiles*: The density profiles for the bulk fluid and the micropore fluid are shown in Figures 7 and 8. We first note that the density profile for the bulk fluid is uniform throughout the pore except from a very narrow region next to the reservoir walls. But even there, the density gradients are entirely insignificant compared to the extremely strong density gradients of the micropore fluid caused by the pore wall potential. Therefore, we conclude that the presence of the reservoirs does not induce any significant structure in the fluid.

The density profile for the micropore fluid is highly structured, showing substantial fluid layering. The local average density profile (see Section 1) of this system is also shown in Figure 8. A very important feature of the local average density that results from the smoothing procedure involved in its calculation is that it varies slowly and remains bound to physically possible homogeneous fluid densities. This is essential if one is to employ some theory for the viscosity of homogeneous fluids to predict local viscosities and flow velocity profiles as explained in Section 1. From Figure 8 we see that the local average density of the micropore fluid is everywhere lower than the hard-sphere closest packing density ($\sqrt{2}/\sigma^3$) and the maximum density for the solution of the Percus-Yevick equation ($6/\pi\sigma^3$).

Although only one density profile is shown in each of Figures 7 and 8 the density profiles of the two systems both at equilibrium and in the presence of flow that have been determined. *A conclusion of great importance that is suggested by the Couette flow simulations is that the density profiles of the two systems in the presence of flow coincide with the equilibrium density profiles, even at the extremely high shear rates employed in our simulation.* A detailed statistical analysis that justifies this point was presented in Reference (5).

ii) *Diffusivities.* Our results for the diffusivities of both systems are summarized in Table I. The pore average transverse diffusivity for the bulk fluid at equilibrium agrees very well with experimental and simulation values for the diffusivity of Argon at the same density and temperature (18,12,5).

As explained in Section 1 three diffusivities were calculated for each system. These were the equilibrium transverse diffusivity and the two nonequilibrium (flow) diffusivities parallel and normal to the direction of flow. As we can see from Table I, they all agree with each other within the limits of statistical uncertainty. *We conclude, therefore, that the flow has no effect on the diffusivity even at such high shear rates as the ones employed in our simulation.* At even higher shear rates a significant dependence of the diffusivity on the shear rate has been reported (19) but one should consider that our shear rate is already orders of magnitude higher than the ones encountered in realistic flow situations.

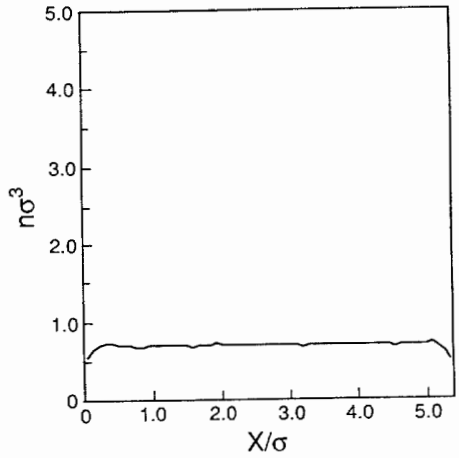

Figure 7. Density profile of the bulk system.

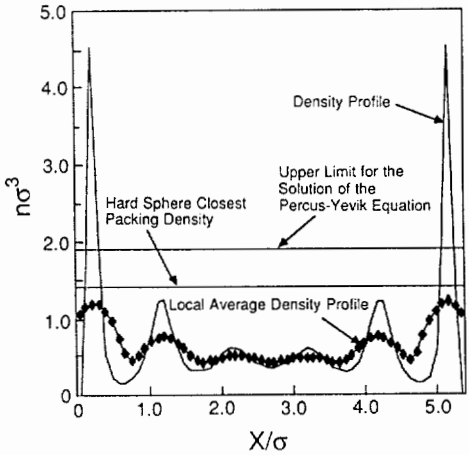

Figure 8. Density and local average density profiles of the micropore fluid

Table I. Diffusivities. Units are $(\sigma^2\epsilon/m)^{1/2}$

	Bulk Fluid	Micropore Fluid
Simulation		
equilibrium	0.109± 0.002	0.107± 0.002
parallel to the flow	0.109± 0.003	0.114± 0.004
normal to the flow	0.109± 0.002	0.113± 0.003
Experiment	0.111	
LADM		
using Enskog theory		0.107
using empirical formula		0.112
Extended Enskog		0.108

As shown in Table I the LADM predictions agree very well with the simulation results. The first of these values employed the Enskog hard-sphere theory for homogeneous fluids for the prediction of the local diffusivities. The second value employed an empirical formula that fits MD results for the diffusivity of liquid Argon (5,18). As we can see much of the disagreement is due to the inaccuracy of the Enskog theory and not to the LADM. The third value is the prediction of the generalization of the Enskog theory for tracer diffusion in strongly inhomogeneous fluids (8,9). This value also agrees very well with the simulation result.

A final point has to do with the relative insensitivity of the pore averaged diffusivity on the density structure. Both the LADM and the generalized tracer diffusion theory provide a rational explanation for this fact. The reasons for the insensitivity may be identified in the double (triple for the tracer diffusion theory) smoothing induced by the volume averaging and by the very nature of the molecular interactions in liquids which makes some type of averaging over the densities in the neighborhood of a certain point necessary.

iii) *Velocity profiles.* The velocity profiles for the bulk fluid and the micropore fluid are shown in Figures 9 and 10. The profile for the bulk system is linear in agreement with the macroscopic prediction of fluid mechanics. This fact shows that the flow properties of our first system are identical with the ones of a bulk fluid, despite the presence of the reservoirs.

The velocity profile for the micropore fluid exhibits large deviations form linearity. An extremely important point which motivated the development of the LADM is the *clear correlation between the velocity and the density profiles of the micropore fluid.* One can easily distinguish two regions of low slope (shear rate) next to the reservoir walls and a center region of high slope. These clearly correspond to the two large density peaks next to each reservoir wall and the low density center region of the density profile. The theoretical velocity profile predicted from the

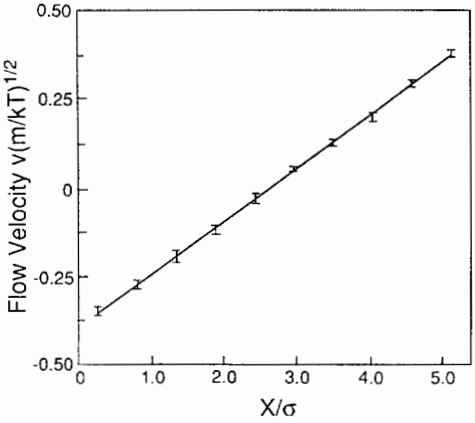

Figure 9. Velocity profile for the bulk system

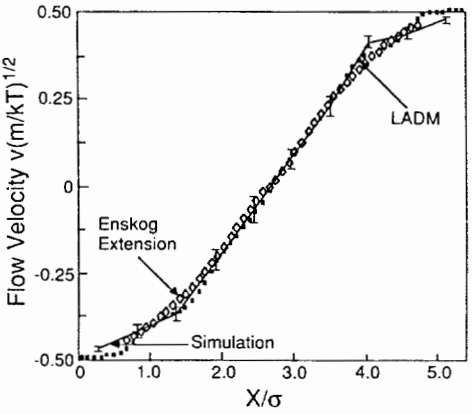

Figure 10. Theoretical and simulation velocity profiles for the micropore fluid.

LADM is also shown in Figure 4. It agrees with the simulation profile almost within the limits of the statistical uncertainty.

In Figure 10, we present flow velocity predictions of the high density approximation, Equations 32 - 33, 38 and 39, of Davis' extension of Enskog's theory to flow in strongly inhomogeneous fluids (10). The velocity profile predicted in this way is also plotted in Figure 10. The predicted profile, the simulated profile, and the profile predicted from the LADM are quite similar.

Finally the knowledge of the velocity profiles allows the determination of the actual shear rate exerted upon the liquid slab. For the bulk system some slip is observed at the reservoir walls. No slip is observed for the micropore fluid as a result of the high density close to the reservoir walls, which facilitates the momentum transfer between the reservoir and the liquid slab particles.

iv) *Shear stress and viscosity.* As explained in Section 1 three independent estimates of the shear stress can be made for this particular type of flow. For both systems they all agree within the limits of statistical uncertainty as shown in Table II. The shear stress in the micropore fluid is significantly lower than the bulk fluid, which shows that *strong density inhomogeneities can induce large changes of the shear stress.*

For the bulk system the constitutive equation

$$\eta = \tau_{xy}/\dot{\gamma} \tag{55}$$

is rigorously valid. The simulation result for the viscosity of the bulk system agrees with the experimental argon viscosity within the limits of the statistical uncertainty.

If one insists on Equation 55 for the micropore fluid an effective viscosity (which is an experimental observable) must be used instead, i.e.,

$$\eta_{eff} = \tau_{xy}/\dot{\gamma} \tag{56}$$

The simulation value for the effective viscosity is almost half the viscosity of the bulk fluid. According to the LADM the effective viscosity for plane Couette flow can be identified as

$$\eta_{eff}^{-1} = s^{-1} \int_0^s [\eta^0(\bar{n}(x))]^{-1} dx \tag{57}$$

where s is the distance between the reservoir walls, $\bar{n}(x)$ the local average density at x (defined by Equation 9), and $\eta^0(\bar{n}(x))$ is the local viscosity at x, i.e., the homogeneous fluid viscosity at density $\bar{n}(x)$

Two predictions of the LADM for the effective viscosity are shown in Table II. The first was made by using the Enskog hard-sphere theory for the calculation of the local viscosities. It agrees qualitatively with the simulation result in that it predicts a large decrease of the effective viscosity as a result of the density structure. For the second prediction the local

Table II. Shear stress and viscosity

Bulk fluid in planar Couette flow			
	Shear Stress	Shear Rate	Viscosity
Simulation			
force on upper reservoir	0.182		
force on lower reservoir	0.180		
Irving-Kirkwood formula	0.181		
average	*0.181± 0.004*	*0.149± 0.005*	*1.21± 0.04*
Experiment			1.23
Enskog			1.14

Micropore fluid in planar Couette flow			
	Shear Stress	Shear Rate	Viscosity
Simulation			
force on upper reservoir	0.119		
force on lower reservoir	0.122		
Irving-Kirkwood formula	0.122		
average	*0.121± 0.003*	*0.186*	*0.65± 0.02*
LADM			
using Enskog theory			0.77
using empirical fit			0.70
Units	ϵ/σ^3	$(\epsilon/m\sigma^2)^{1/2}$	$(m\epsilon)^{1/2}\sigma^2$

viscosities were calculated from an empirical formula (23) that fits experimental value of the argon shear viscosity over a wide range of densities and temperatures (20,21). The agreement with the simulation result is much better, which suggests that much of the discrepancy is a result of the poor Enskog predictions at high densities and not a deficiency of the LADM.

A final comment has to do with the concept of effective viscosity in strongly inhomogeneous fluids. For these systems the definition of the effective viscosity depends on the type flow, hence different effective viscosities will be measured for different flow situations in the same system with the same density profile. Therefore, the effective viscosity is a concept of limited value and measurements of this quantity do not provide much information about the effects of density structure on the flow behavior.

Literature Cited

1. Fischer, J.; Methfessel, M. *Phys. Rev A* 1980 **22**, 2836.
2. Carnahan, N. F. ; Starling, K. E. *J. Chem. Phys.* 1969 **51**, 635.
3. Steele, W. A., *The Interaction of Gases with Solid Surfaces* Pergamon, New York, 1974; Chap. 2.

4. Horn, R. G. ; Israelachvili, J. N. *J. Chem. Phys.* 1981 **75**, 1400
5. Bitsanis, I.; Tirrell, M. V.; Davis, H. T. *J. Chem. Phys.* (accepted).
6. Dymond, J. H.; Woolf, L. A. *J. Chem. Soc. Faraday Trans. 1* 1982 **78**, 991.
7. Chapman, S.; Cowling, T. G. *The Mathematical Theory of Non-Uniform Gases and Liquids*, Cambridge University Press, New York, 1954.
8. Davis, H. T., *J. Chem. Phys.* (accepted).
9. Vanderlick, T. K.; Davis, H. T. *J. Chem. Phys.* (accepted).
10. Davis, H. T., *Chem. Eng. Comm.* (accepted).
11. Luks, K.D.; Miller, M.; Davis, H. T. *AIChE J.* 1966 **12**, 1079.
12. Magda, J. J.; Tirrell, M. V.; Davis, H. T. *J. Chem. Phys.* 1985 **83**, 1888.
13. Snook, I. K.; van Megen, W. *J. Chem. Phys.* 1980 **72**, 2907.
14. Beeman, D. *J. Comput. Phys.* 1976 **20**, 130.
15. Irving, J. H.; Kirkwood, J. G. *J. Chem. Phys.* 1950 **18**, 817.
16. Ashurst, W. T.; Hoover, W. G. *Phys. Rev. A* 1975 **11**, 658.
17. Heyes, D. M.; Montrose, C. J.; Litovitz, T. A. *J. Chem. Soc. Faraday Trans. 2* 1983 **79**, 611.
18. Levesque, D.; Verlet, L. *Phys. Rev. A* 1970 **6**, 2514.
19. Heyes, D. M. *J. Chem. Soc. Faraday Trans. 2* 1985**82**, 1365.
20. Haynes, W. M. *Physica* 1973 **67**, 440.
21. Michels, A.; Sengers, J. V.; van der Klundert, L. J. M., *Physica* 1963 **29**, 149.

RECEIVED June 15, 1987